JACS
JOURNAL OF THE AMERICAN CHEMICAL SOCIETY
Article
pubs.acs.org/JACS

# Solution-Cast Metal Oxide Thin Film Electrocatalysts for Oxygen Evolution

Lena Trotochaud, James K. Ranney, Kerisha N. Williams, and Shannon W. Boettcher*

Department of Chemistry and the Center for Sustainable Materials Chemistry, University of Oregon, Eugene, Oregon 97403, United States

Supporting Information

**ABSTRACT:** Water oxidation is a critical step in water splitting to make hydrogen fuel. We report the solution synthesis, structural/compositional characterization, and oxygen evolution reaction (OER) electrocatalytic properties of ~2−3 nm thick films of $NiO_x$, $CoO_x$, $Ni_yCo_{1-y}O_x$, $Ni_{0.9}Fe_{0.1}O_x$, $IrO_x$, $MnO_x$, and $FeO_x$. The thin-film geometry enables the use of quartz crystal microgravimetry, voltammetry, and steady-state Tafel measurements to study the electrocatalytic activity and electrochemical properties of the oxides. $Ni_{0.9}Fe_{0.1}O_x$ was found to be the most active water oxidation catalyst in basic media, passing 10 mA $cm^{-2}$ at an overpotential of 336 mV with a Tafel slope of 30 mV $dec^{-1}$ with oxygen evolution reaction (OER) activity roughly an order of magnitude higher than $IrO_x$ control films and similar to the best known OER catalysts in basic media. The high activity is attributed to the *in situ* formation of layered $Ni_{0.9}Fe_{0.1}OOH$ oxyhydroxide species with nearly every Ni atom electrochemically active. In contrast to previous reports that showed synergy between Co and Ni oxides for OER catalysis, $Ni_yCo_{1-y}O_x$ thin films showed decreasing activity relative to the pure $NiO_x$ films with increasing Co content. This finding is explained by the suppressed *in situ* formation of the active layered oxyhydroxide with increasing Co. The high OER activity and simple synthesis make these Ni-based catalyst thin films useful for incorporating with semiconductor photoelectrodes for direct solar-driven water splitting or in high-surface-area electrodes for water electrolysis.

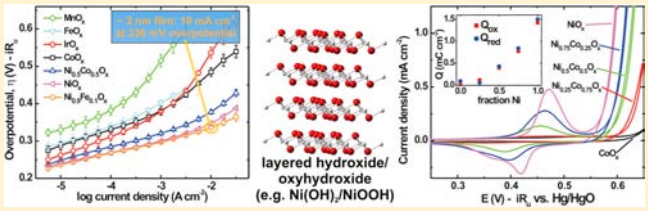


## 1. INTRODUCTION

The electrolysis of water to form hydrogen and oxygen gas (i.e., water splitting, $H_2O \rightarrow H_2 + 1/2O_2$) provides a possible pathway for the large-scale storage of intermittent energy from the sun, wind, or other renewable sources.[1,2] The oxygen evolution reaction (OER) $2H_2O \rightarrow 4H^+ + O_2 + 4e^-$ (in acidic media) or $4OH^- \rightarrow 2H_2O + O_2 + 4e^-$ (in basic media) is kinetically slow and hence represents a significant efficiency loss in both electricity-driven and photodriven water splitting.[2,3] Understanding the relationships between catalyst architecture, composition, and activity is critical for the development of catalysts with higher activities.

The early work on OER electrocatalysis has been reviewed by Trasatti[4] and Matsumoto.[5] The majority of this work was performed on thick electrodes fashioned by the hot-pressing of bulk powders or on electrodeposited films many micrometers thick. Such poorly defined porous architectures make comparisons of different materials difficult as the measured catalytic response is influenced by the active surface area and the electron/mass transport properties in a manner that is difficult to correct for.[6] It has been noted that this is a key limitation in comparing experimental data with theoretical predictions.[7] Limited work has been performed on single crystals,[8,9] yet even when single crystals are available, differences in electronic properties can prevent identification of the basic relationships between structure, composition, and electrocatalytic activity. Despite these limitations, Trasatti formed a useful volcano relation by correlating the activities of the catalysts with the enthalpy of a lower to higher oxide transition and concluded that $IrO_2$ and $RuO_2$ are the most active OER electrocatalysts.[10] Recent density functional theory calculations by Rossmeisl et al. have attributed the high activity of these precious metal catalysts to the near thermochemical equivalence of each elementary step in the oxidation reaction.[11,12] First-row transition-metal oxides containing Ni, Co, and Mn are typically considered to be of lower activity because the M−O bond strength is either too strong or too weak, thereby slowing the rate-limiting step.[7] Recently Subbaraman et al. studied electrodeposited metal hydroxide catalysts on Pt single crystals and also found that the oxophilicity of the metal cation (i.e., the M−OH bond strength) correlates with activity.[13] Nocera and co-workers have found evidence for the formation of such metal hydroxides in electrodeposited Ni-borate catalyst films.[14] Other reports indicate that mixed oxides, for instance, $LaNiO_3$ and $NiCo_2O_3$, have higher activities than single-component oxides of the same elements.[15,16] Suntivich et al. reported the activities of a variety of perovskite electrocatalyst powders and found that the surface cation $e_g$ orbital occupation correlated with the observed OER activity.[3] They used this descriptor to identify a perovskite catalyst, $Ba_{0.5}Sr_{0.5}Co_{0.8}Fe_{0.2}O_{3-\delta}$, with higher specific surface-

**Received:** July 30, 2012
**Published:** September 19, 2012

  

area activity than $IrO_2$. The measurements were made using a rotating-disk electrode with well-defined oxygen transport,[17] with the perovskite powders supported in a conducting carbon/Nafion composite film on the electrode surface. The surface areas of the catalyst powders were estimated from scanning electron microscopy (SEM) measurements so that the specific surface-area activities could be compared. The disadvantages of this technique are the potential for the background oxidation of the conductive C at high current densities and the difficulty in processing powder-based catalysts into high-surface-area electrode architectures or combining them with semiconductors for light-driven water splitting.

Herein we report the solution synthesis of ultrathin film metal oxide electrocatalysts onto quartz crystal microbalance electrodes where the mass is measured and monitored *in situ*. The films are spun cast from alcohol solutions of metal salts mixed with surfactant to reduce surface tension and promote film formation. Quick (~2 min), low-temperature (~300 °C) annealing decomposes the nitrate anions and surfactant leaving a ~2−3 nm thick layer of the desired oxide on the conductive electrode surface. The films are useful for fundamental study for the following reasons: (1) The electrocatalyst conductivity does not significantly influence the measured overpotential because electrons must move only the thin-film thickness to reach the support electrode as opposed to $\mu$m to mm through a pellet, crystal, or thick layer. (2) Many of the oxide electrocatalysts are semiconductors, and Schottky barriers at the catalyst−solution and catalyst−metal electrode interfaces can impede electron transport and result in an additional overpotential that is dependent on the carrier concentration (i.e., doping) in the semiconductor.[5] Films <5 nm thick are not thick enough to support a large depletion region and therefore catalysis should be comparable independent from carrier concentration and interfacial contact properties. (3) The film composition can be exactly controlled by the metal ions added to the precursor solution. Compositions that are not accessible via traditional high-temperature routes (e.g., due to phase separation) or electrodeposition can be made. (4) Variations in real vs geometric surface area (i.e., roughness factors) of high-surface-area electrodes are difficult to accurately correct for.[18] Ultrathin films prepared from solution should have similar roughness factors that are at most a few times larger than unity. (5) The mass transport of evolving gases is facile due to lack of extensive porous structure.

We use the thin film synthesis techniques developed here to quantitatively compare the OER activity of $NiO_x$, $CoO_x$, $Ni_yCo_{1-y}O_x$, $Ni_{0.9}Fe_{0.1}O_x$, $IrO_x$, $MnO_x$, and $FeO_x$ catalysts, to study the films' electrochemical behavior, and to follow changes in the active catalyst structure during the OER. We show that $Ni_{0.9}Fe_{0.1}O_x$ is one of the best catalysts in basic media with OER catalytic activity more than 10-fold higher than $IrO_x$ depending on the applied potential. We characterize the *in situ* transformation of the deposited Ni-containing films to redox active Ni hydroxide/oxyhydroxide phases which are identified as the active catalyst. These thin film OER catalysts are practically useful because the solution deposition techniques can be used to couple them with semiconductor photoelectrodes for sunlight-driven water splitting as well as to incorporate them into optimized high-surface-area electrodes for traditional water electrolysis applications.

## 2. EXPERIMENTAL SECTION

**2.1. Preparation of Thin Film Precursor Solutions.** Precursor solutions were prepared by dissolving metal nitrates [$Ni(NO_3)_2{\cdot}6H_2O$, 98% Alfa-Aesar; $Co(NO_3)_2{\cdot}6H_2O$, 98+% Sigma-Aldrich; $Fe(NO_3)_3{\cdot}9H_2O$, Mallinckrodt analytical grade; $Mn(NO_3)_2{\cdot}4H_2O$, 97+% Sigma-Aldrich] in ethanol at a concentration of 0.05 M. Triton X-100 (J.T. Baker) was added to give 0.15 g Triton per mmol of metal ions. For mixed-metal films, the salts were combined in the desired molar ratio to a total metal ion concentration of 0.05 M. Iridium chloride ($IrCl_3{\cdot}xH_2O$, 99.9% Strem Chemicals) was used to make the $IrO_x$ precursor solution. The $IrCl_3$ solutions were prepared at 0.025 M to ensure complete dissolution (with 0.15 g Triton/mmol Ir). The colored precursor solutions containing Ir, Co, Ni, and Co/Ni mixtures were stable indefinitely. The clear Mn precursor solution was stable for 2−3 weeks if not exposed to direct sunlight. A brown precipitate, presumably MnOOH,[19] was observed after prolonged time and/or sunlight exposure. The yellow-orange $Fe(NO_3)_3$ solutions began to form an orange-brown precipitate after ~4 h due to formation of FeOOH.[19] Precursor solutions containing Fe were thus freshly prepared before each film deposition.

**2.2. Thin Film Deposition and Annealing.** Metal-oxide and mixed-metal-oxide thin films were deposited from precursor solutions by spin coating. Substrates, including Au/Ti QCM crystals (Stanford Research Systems), Si, indium-doped tin-oxide-coated glass (ITO, Delta Technologies), and Au/Ti-coated glass slides, were cleaned prior to deposition by ultrasonication for 30 min in a 6.25% (v/v) solution of Contrad-70 detergent (Decon Laboratories) in 18.2 MΩ cm ultrapure water at 45 °C, rinsed with ultrapure water, and dried by spinning at 5000 rpm for 90 s. Approximately 0.25 mL of precursor solution was cast onto a substrate which was then spun at 5000 rpm for 90 s. The films were annealed in air on a hot plate at 300 °C for 2 min for the thin QCM and Si substrates or 5 min for the thicker substrates.

**2.3. Characterization.** Microgravimetry measurements were made using a 5 MHz quartz crystal microbalance (Stanford Research Systems QCM200). The film mass was calculated from changes in resonance frequency using the Sauerbrey equation[20] $\Delta f = -C_f \times \Delta m$, where $\Delta f$ is the observed frequency change (Hz), $C_f$ is the sensitivity factor of the 5 MHz AT-cut quartz crystal (58.3 ± 3.7 Hz $\mu g^{-1}$ $cm^2$; see SI for description of $C_f$ calibration), and $\Delta m$ is the change in mass per unit area ($\mu g$ $cm^{-2}$). The total metal ion content of the thin films was determined from microbalance measurements of the dry films assuming full oxygen stoichiometry of the thermodynamically stable oxides, e.g. NiO, $Co_3O_4$, $MnO_2$, $IrO_2$, $Fe_3O_4$.

Grazing incidence X-ray diffraction (GIXRD) patterns were recorded on a Phillips X'Pert Panalytical diffractometer operating at 40 mA and 45 kV using monochromated Cu $K\alpha_1$ radiation (incident angle = 0.5°, $\lambda$ = 1.541 Å, step size = 0.5°, integration time 20 s/step). SEM images were collected on a Zeiss Ultra 55 SEM at 5 kV. Samples for SEM imaging were deposited on Si wafers (the roughness of evaporated Au or ITO substrates made imaging the thin films difficult; see SI for images).

X-ray photoelectron spectroscopy (XPS) studies were carried out on an ESCALAB 250 (ThermoScientific) using an Al $K\alpha$ monochromated (150 W, 20 eV pass energy, 500 $\mu$m spot size) or a Mg $K\alpha$ nonmonochromated flood (400 W, 75 eV pass energy) source. The samples were charge-neutralized using an in-lens electron source combined with a low-energy $Ar^+$ flood source. Spectra were analyzed using ThermoScientific Avantage 4.75 software. The Au $4f_{7/2}$ signal at 84.0 eV was used to calibrate the binding energy scale.

Electron probe microanalysis (EPMA) was performed using a Cameca SX-100 equipped with five tunable wavelength dispersive spectrometers. Operating conditions were 40° takeoff angle, beam current 20 nA, and 50 $\mu$m spot size, with data collected at three different accelerating voltages (10, 15, and 20 keV). Experimental intensities were determined from the average of eight proximate positions on each sample. The exponential or polynomial background fit was utilized.[21] Quantitative elemental analysis was determined by

comparing experimental *k*-ratios to simulated values using Stratagem thin film composition analysis software.[22]

**2.4. Electrochemical Measurements.** Electrochemical measurements were made in a cylindrical glass cell (see Figure S1) containing ~150 mL of 1 M KOH electrolyte solution (Fluka Analytical TraceSelect, ≥ 30%, diluted with 18.2 MΩ cm water) using a PARSTAT 2273 potentiostat operating in standard three-electrode mode. A Pt mesh separated by a 2 cm diameter medium-porosity glass frit was used as a counter electrode. All potentials were measured vs a 1 M KOH Hg/HgO reference electrode (CH Instruments) housed in a custom glass Luggin capillary. The tip of the Luggin capillary was positioned ~1−2 mm from the surface of the working electrode to minimize uncompensated solution resistance, $R_u$. Samples deposited on QCM electrodes were connected to the working electrode lead of the potentiostat through the crystal face bias connector of the QCM200. Working electrodes for samples deposited on Au/Ti or ITO coated glass were fabricated by contacting a wire to the sample surface using Ag paint. Ag paint was also applied around the edges of the ITO to minimize series resistance. The Ag paint was then sealed in inert epoxy (Loctite Hysol 1C) along with the contacting wire that was fed through a glass tube. Control experiments showed no background current from the epoxy. No significant differences in electrochemical response were observed for samples deposited on QCM, Au/Ti-coated glass, or ITO-coated glass electrodes. Data presented in the text represent measurements made on QCM electrodes unless otherwise indicated.

The potential of the 1 M KOH Hg/HgO reference electrode was measured to be 0.929 V vs the reversible hydrogen electrode (RHE) at pH 14 (i.e., 0.112 V vs NHE). The RHE was fabricated by bubbling high-purity hydrogen over a freshly cleaned Pt mesh in 1 M KOH. Ultrahigh-purity $O_2$ gas was bubbled through the solution for at least 20 min prior to and throughout electrochemical measurements. Magnetic stirring was used to dislodge $O_2$ bubbles formed on the electrode surface. All electrochemical data was corrected for $R_u$, which was determined by equating $R_u$ to the minimum total impedance in the frequency regime between 10 and 50 kHz, where the capacitive and inductive impedances are negligible and the phase angle was near zero. $R_u$ was 0.2−2 Ω for gold-coated substrates and ~1−5 Ω for ITO substrates. $R_u$ was also determined by the current-interrupt method, but that was found to overestimate $R_u$ leading to nonphysical Tafel plots. The overpotential $\eta$ was calculated using the equation $\eta = E_{measured} - E_{rev} - iR_u$, where $E_{measured}$ is the potential recorded vs Hg/HgO, $E_{rev}$ is the reversible potential of the OER vs Hg/HgO (0.30 V at pH 14), and $i$ is the current. Current densities are calculated using geometric surface areas.

## 3. RESULTS AND DISCUSSION

**3.1. $Ni_yCo_{1-y}O_x$ Mixed Oxides: A Case Study in Ultrathin Film Catalysis.** $Ni_yCo_{1-y}O_x$ has been reported to be one of the most active nonprecious metal catalysts for the OER with optimized materials exhibiting Tafel slopes between 40 and 60 mV $dec^{-1}$.[23−28] However, the catalytic activity of these materials appears highly dependent on a number of experimental factors, including the synthetic method and product morphology,[25−30] aging and cycling of the electrode,[29,30] and type of electrode substrate.[27] The mechanism for the reported performance enhancement for the mixed oxide relative to $NiO_x$ or $CoO_x$ is unclear. We have therefore studied $Ni_yCo_{1-y}O_x$ OER catalysts in the thin-film geometry to provide new insight into the activity trends in the absence of confounding effects associated with high-surface-area or thick-film architectures.

*3.1.1. Characterization of As-Deposited Films.* Following spin-casting of the metal oxide precursor solution, microbalance measurements showed that >85% of the original film mass was lost during the first minute of heating at 300 °C due to the removal of nitrate, ethanol, and surfactant (Figure S2). Between 2 and 6 min at 300 °C, no further mass loss was measured. XPS analysis showed no N in the annealed films, confirming the complete combustion of the nitrate salts (a discussion of the XPS analysis of trace impurities can be found in the SI). Figure 1 shows representative SEM images taken of $Ni_yCo_{1-y}O_x$ thin

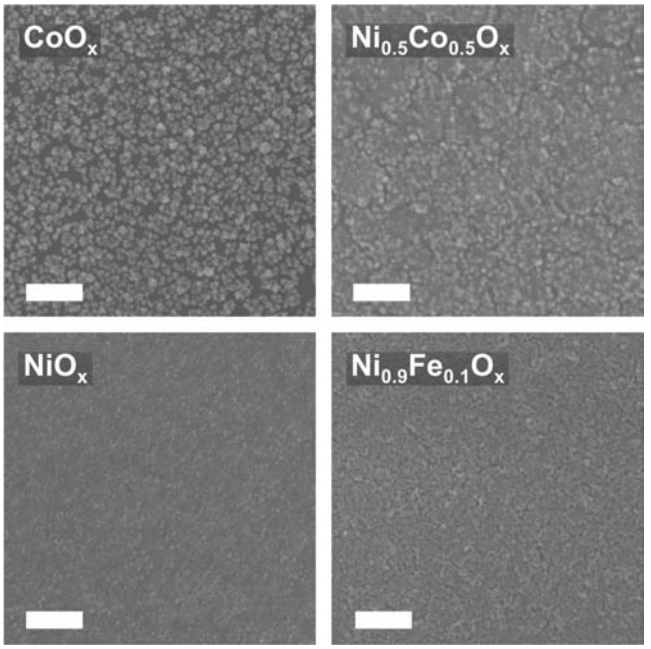


**Figure 1.** SEM images of select thin films prepared on Si by the solution deposition method. Scale bars are 100 nm.

films (and a $Ni_{0.9}Fe_{0.1}O_x$ film to be discussed later) showing uniform coverage across the sample surface. At high magnification, nanoscale texturing of the film surface is apparent, with the $CoO_x$ films more highly textured than the $NiO_x$ films. Additional SEM images of films can be found in Figures S3−S5. Average film thicknesses, determined from the film mass and density of the known oxide phases, ranged from 1.6 to 2.5 nm. Cross-sectional TEM analysis of the $NiO_x$ films deposited on the Au/Ti electrodes confirmed an average thickness of ~2 nm (Figure S6).

Grazing incidence XRD shows reflections corresponding to spinel $Co_3O_4$ and rock salt NiO for the $CoO_x$ and $NiO_x$ films, respectively (Figure 2). For $Ni_yCo_{1-y}O_x$ films, only one set of reflections is observed in each sample. For $y$ = 0.25, reflections consistent with the spinel structure are observed. For $y$ = 0.5 and 0.75, reflections for the rock salt structure are observed. For the $y$ = 0.5 sample, the reflection centered at 63.7° 2$\theta$ lies between that of NiO (220) and $Co_3O_4$ (440) (at 62.9° 2$\theta$ and 65.2° 2$\theta$, respectively). The lack of clear NiO (220) and $Co_3O_4$ (440) reflections suggests a single mixed $Ni_yCo_{1-y}O_x$ phase is present, as opposed to a phase separated mixture of the Ni and Co oxides, although a conclusive analysis is limited by the low intensity of the peaks for these ultrathin film samples.

*3.1.2. Cyclic Voltammetry (CV) and the Effects of Electrochemical Conditioning.* Figure 3 shows a series of cyclic voltammograms collected for a $NiO_x$ film during several hours of galvanostatic conditioning at an anodic current density of 10 mA $cm^{-2}$. The as-deposited film shows a small reversible wave due to Ni redox processes, and OER current reaches 1 mA $cm^{-2}$ at $\eta$ = 324 mV. After 1 h at 10 mA $cm^{-2}$, a wave corresponding to $Ni^{2+}$ oxidation centered at 472 mV vs Hg/


dx.doi.org/10.1021/ja307507a | J. Am. Chem. Soc. 2012, 134, 17253−17261

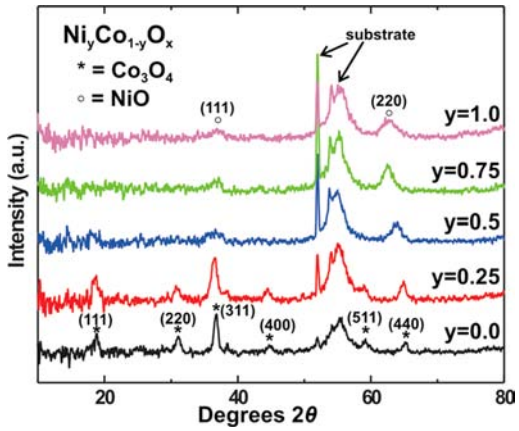


**Figure 2.** Grazing incidence XRD patterns of $CoO_x$, $Ni_yCo_{1-y}O_x$, and $NiO_x$ films. Films were prepared by five consecutive depositions onto Si substrates. Patterns have been referenced to the sharp peak at 52° 2$\theta$, which is an artifact of the single crystalline (100) Si substrate wafers. The broad feature centered at 55° 2$\theta$ is also an artifact of the (100) Si substrate. The sloping background due to the grazing incidence geometry has been subtracted for clarity (see Figure S7).

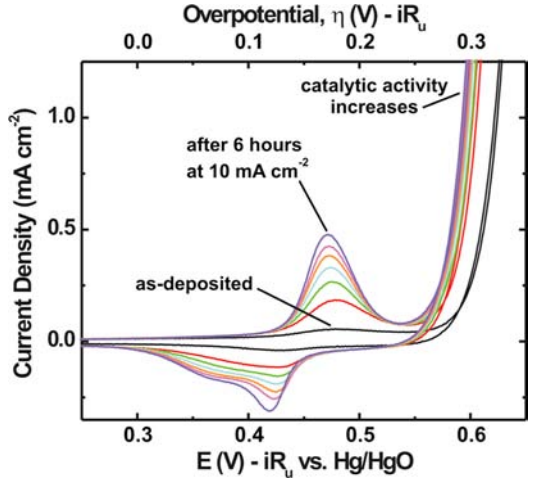


**Figure 3.** Cyclic voltammograms of a $NiO_x$ film during electrochemical conditioning collected at a scan rate of 20 mV $s^{-1}$ in 1 M KOH. After collection of the initial (as-deposited) scan, subsequent scans were collected at 1 h intervals during anodic galvanostatic conditioning at 10 mA $cm^{-2}$.

HgO is observed. A corresponding broad reduction wave near 420 mV vs Hg/HgO is also present, and the overpotential required for 1 mA $cm^{-2}$ OER current has decreased to $\eta$ = 302 mV (as discussed below, $\eta$ is remarkably small given the minimal catalyst loading). As electrochemical conditioning continues, CV scans collected every hour show that the $Ni^{2+}$ oxidation wave increases in area and that the OER activity increases. Typically, after 6 h of conditioning, no large changes were observed in subsequent CV scans with additional conditioning. Integration of the total charge under the $Ni^{2+}$ oxidation wave after 6 h of conditioning (1.5 mC $cm^{-2}$) in combination with QCM mass measurements ($9.4 \times 10^{15}$ Ni $cm^{-2}$) indicates that nearly all of the Ni centers in the film are electrochemically active (~1 electron per Ni). We note that some studies have assigned this wave to a $Ni^{2+}/Ni^{+3.67}$ redox process implying an ultimate limit of 1.67 $e^-$ per Ni as opposed to the simple 1 electron $Ni^{2+}/Ni^{3+}$ process.[31]

The changes in the $NiO_x$ film voltammetry are attributed to the *in situ* formation of $Ni(OH)_2$/NiOOH hydroxide/oxyhydroxide species during the electrochemical conditioning process, which is depicted in Figure 4. The observed $Ni^{2+}$

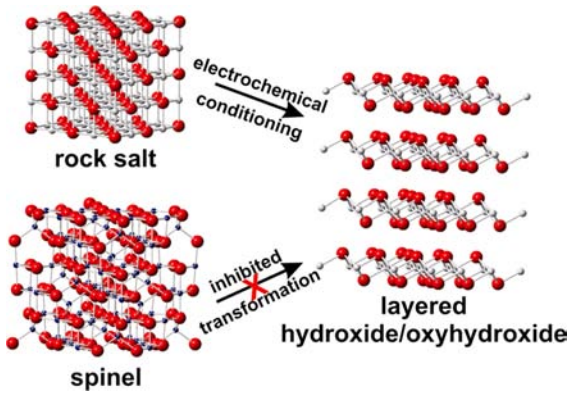


**Figure 4.** Proposed *in situ* transformation from the thermally prepared oxides to the layered hydroxide/oxyhydroxide structure as discussed in the text.

oxidation wave at 472 mV vs Hg/HgO is assigned to the reversible $Ni(OH)_2$/NiOOH redox reaction.[32−34] Unlike the redox activity of the as-deposited NiO films which is limited to the surface Ni atoms, the layered $Ni(OH)_2$/NiOOH structure is composed of weakly interacting hydroxide layers that allow the intercalation of water and anions and therefore bulk redox activity (enabling also use in rechargeable battery electrodes).[34] The decrease in OER overpotential with increasing conversion of NiO to NiOOH indicates that the NiOOH is the active catalyst for OER. The $Ni^{2+}$ oxidation wave for conditioned $NiO_x$ films shifted to higher potentials after soaking in KOH solutions for several hours (Figure S8). This observation is consistent with the conversion of the disordered $\alpha$-$Ni(OH)_2$ formed after electrochemical conditioning (i.e., in the resting state of the catalyst) to the ordered $\beta$-$Ni(OH)_2$ polymorph upon aging in base, as has been observed previously.[34]

Evidence for the proposed *in situ* transformation is found by comparing XPS spectra of the $NiO_x$ film before and after electrochemical conditioning. In the Ni 2p region (Figure 5a), the as-deposited $NiO_x$ film shows three main peaks for Ni $2p_{3/2}$ at binding energies of 853.2, 855.1, and 860.2 eV. After electrochemical conditioning, peaks at 856.1 and ~862 eV are observed. These spectral differences indicate a transformation from NiO to $Ni(OH)_2$ that is consistent with the known Ni $2p_{3/2}$ XPS spectra of NiO and $Ni(OH)_2$.[35−37] A change in binding environments can also be seen in the O 1s XPS region (Figure 5b). The as-deposited $NiO_x$ film shows two predominant peaks at 529.1 and 530.9 eV, while the conditioned film shows one peak at 531.7 eV. This is consistent with previous studies that compare the O 1s XPS spectra of NiO and $Ni(OH)_2$ samples.[35,37] The lower energy peak in the NiO spectrum is attributed to O-vacancy lattice defects.[35,37] The absence of these two peaks at lower binding energy in the conditioned sample indicates conversion to $Ni(OH)_2$. XPS analysis also shows the presence of Fe in the conditioned films, which originates from electrolyte impurities and could play an important role in the catalysis. We discuss the presence and influence of Fe below.

Similar changes in voltammetry with conditioning were observed for all samples containing Ni (Figure S9). Figure 6


dx.doi.org/10.1021/ja307507a | J. Am. Chem. Soc. 2012, 134, 17253−17261

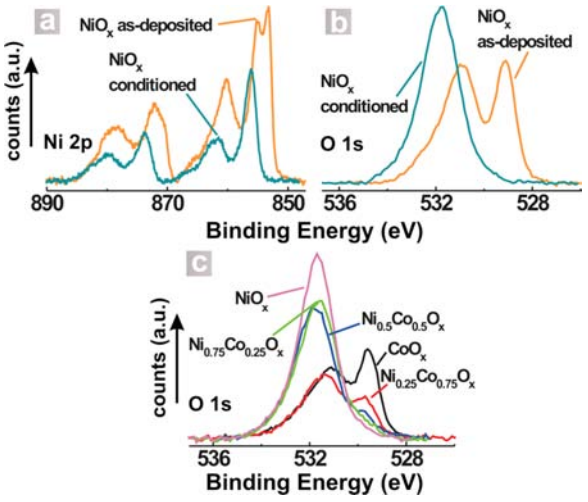


**Figure 5.** Comparison of the Ni 2p (a) and O 1s (b) XPS spectra of a $NiO_x$ thin film before and after electrochemical conditioning. Electrochemically conditioned samples were driven to 0.2 V vs Hg/HgO prior to XPS analysis. (c) Evolution of the O 1s peak for the conditioned $Ni_yCo_{1-y}O_x$ samples. The background signal has been subtracted from all spectra.

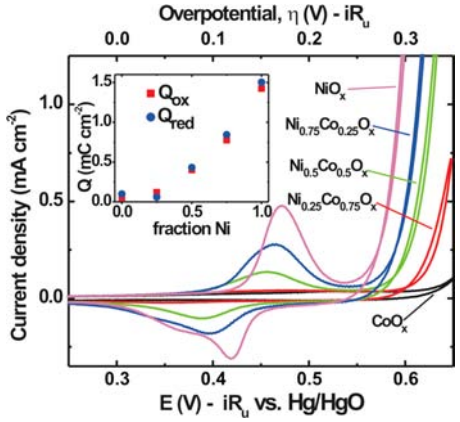


**Figure 6.** Voltammetry of the conditioned $NiO_x$, $Ni_yCo_{1-y}O_x$, and $CoO_x$ films collected in 1 M KOH at a scan rate of 20 mV $s^{-1}$. All films containing Ni show an increase of the $Ni^{2+}$ oxidation wave after electrochemical conditioning compared to the as-deposited films. Inset: Integrated charge Q for the redox processes as a function of Ni content. A linear background was subtracted for peak integration to correct for background capacitance and OER onset current (see Figure S10).

shows cyclic voltammograms for $Ni_yCo_{1-y}O_x$ films each conditioned for 6 h at 10 mA $cm^{-2}$. The potential experienced by the Ni-containing films during conditioning was initially near $\eta$ = 0.6−0.7 V and gradually decreased to $\eta$ = 0.3−0.4 V after 6 h. The voltammetry of the $CoO_x$ thin film did not change with conditioning. With increasing values of $y$, the conditioned $Ni_yCo_{1-y}O_x$ films showed increased $Ni(OH)_2$/NiOOH redox activity as well as decreases in overpotential required for oxygen evolution. Integrated charge for the oxidation and reduction waves ($Q_{ox}$ and $Q_{red}$) are plotted vs Ni content in the inset of Figure 6. Table 1 compares the integrated charge for each film (the average of $Q_{ox}$ and $Q_{red}$) normalized by the total metal ion content as well as Ni content in each film determined from microbalance measurements of the dry films. With increasing Co, the fraction of electrochemically active Ni decreases. As all of the Ni centers would be electrochemically accessible upon

**Table 1. Integrated Charge for $Ni_yCo_{1-y}O_x$ Films[a]**

| sample | dry mass ($\mu$g) | $e^-$ per metal | $e^-$ per Ni |
|---|---|---|---|
| $CoO_x$ | 1.82 | 0.04 | n/a |
| $Ni_{0.25}Co_{0.75}O_x$ | 1.54 | 0.07 | 0.27 |
| $Ni_{0.5}Co_{0.5}O_x$ | 1.46 | 0.31 | 0.63 |
| $Ni_{0.75}Co_{0.25}O_x$ | 1.44 | 0.61 | 0.82 |
| $NiO_x$ | 1.56 | 1.00 | 1.00 |

[a]All values are ± ~10% due to uncertainties in mass measurements (see SI for details).

the full conversion to the layered hydroxide phases, these results indicate that the addition of Co suppresses the *in situ* transformation from oxide to layered hydroxide.

Analysis of the XPS O 1s spectra supports the hypothesis that Co suppresses the formation of the layered hydroxide phase. Figure 5c shows the O 1s peak for the $Ni_yCo_{1-y}O_x$ samples after conditioning at 10 mA $cm^{-2}$ for 6 h. After accounting for adventitious oxygen−carbon species (see Figure S11 for details and peak fits), the spectra are fit well by one or two peaks attributed to metal−oxygen species. These peaks, centered near 529.6 and 531.7 eV, are assigned to metal oxide (spinel) and metal hydroxide (brucite) species, respectively, based on previous studies of Co and Ni oxides and hydroxides.[35−39] The spectrum of the $CoO_x$ sample contains the spinel peak and an additional peak at 531.1 eV, which is attributed to surface O defects in the $Co_3O_4$ spinel.[38,39] As the Ni content of the films is increased, the spinel peak diminishes, and the brucite peak increases in intensity. Even for samples with 75% Ni, a small shoulder near 529.6 eV shows that the complete transformation to the layered hydroxide structure is prevented.

*3.1.3. Quartz Crystal Microgravimetry.* During electrochemical measurements, films deposited on quartz crystals were monitored for mass changes. No mass loss was observed, indicating that the films did not dissolve or degrade in solution. For example, the QCM resonance frequency for as-deposited $CoO_x$ and the electrochemically conditioned $CoO_x$ was constant to within a few Hz (i.e., ± 0.05 $\mu$g $cm^{-2}$). For films containing Ni, the film mass increased significantly (1.3−1.9 $\mu$g $cm^{-2}$) during electrochemical conditioning, such that the final mass was around twice that of the initial as-deposited film. The increase in mass after electrochemical cycling for $NiO_x$ and $Ni_yCo_{1-y}O_x$ films is consistent with several processes,[34] including conversion from the as-deposited oxide NiO (MW = 74.69 g $mol^{-1}$) to the hydroxide $Ni(OH)_2$ (MW = 92.72 g $mol^{-1}$), incorporation of iron impurities (see Section 3.1.4), and intercalation of water between the layered hydroxide sheets. The ability to both quantify the precise mass of the initial dry deposited films and confirm that the ultrathin films are stable under operational conditions using electrochemical QCM measurements is important for comparing and understanding the observed OER activities.

*3.1.4. Catalytic Activity of the $Ni_yCo_{1-y}O_x$ System and the Role of Fe Impurities.* Steady-state Tafel measurements for the $Ni_yCo_{1-y}O_x$ films are presented in Figure 7. Tafel slopes were fit to the linear region of the data below 1 mA $cm^{-2}$. Consistent with the voltammetry measurements (Figure 6), the overpotential decreases as the Ni content of the film increases. $CoO_x$ shows the highest overpotentials and Tafel slope (42 mV $dec^{-1}$), while $NiO_x$ shows the lowest overpotentials and Tafel slope (29 mV $dec^{-1}$). No synergistic effect is apparent upon mixing of the two oxides, and the activity simply decreases as


dx.doi.org/10.1021/ja307507a | J. Am. Chem. Soc. 2012, 134, 17253−17261

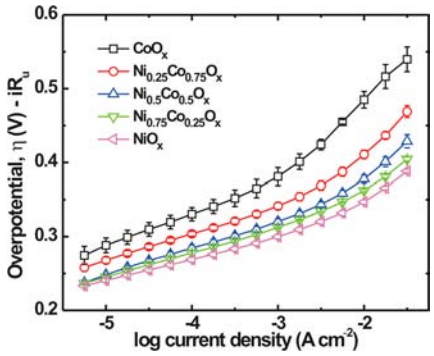


**Figure 7.** Steady-state Tafel measurements for conditioned $NiO_x$, $Ni_yCo_{1-y}O_x$, and $CoO_x$ films collected in 1 M KOH. Each data point represents a galvanostatic measurement held for at least 15 min and is the average of three different electrode samples (1 QCM and 2 Au/Ti-coated glass electrodes). Note that some error bars are smaller than the symbols.

Co is added to $NiO_x$, in contrast with previous reports on electrodes with higher surface area.[23−27,40] The data are consistent with the hypothesis shown in Figure 4, where the rock salt NiO undergoes an *in situ* transformation to the layered hydroxide/oxyhydroxide phase, while the initial presence of Co that favors the spinel-type oxide inhibits this transformation. Because the ultrathin film architectures studied here are essentially "all surface", the observed electrochemical response is particularly sensitive to these changes. These observations could also be important for understanding previously studied $Ni_yCo_{1-y}O_x$ systems,[23−27,40] where similar chemical changes are likely occurring at the outer surfaces of the particulate catalysts but perhaps are masked by the various convoluting factors associated with catalysis measurements on porous electrodes mentioned earlier. After formation of the hydroxide/oxyhydroxide catalyst during conditioning, the $NiO_x$ films are remarkably active, passing 20 mA cm$^{-2}$ at an overpotential of 370 mV despite having an average thickness of only ∼2 nm.

Previous work by Corrigan on electrochemical cycling of thicker (0.5 mg cm$^{-2}$) electrodeposited $Ni(OH)_2$ films has shown that Fe impurities in KOH electrolyte solutions increase OER activity.[32] The catalytic activity of thinner films (50 μg cm$^{-2}$) was shown to be affected more than thicker films, as the relative fraction of Fe in the thinner film was greater. The effects were similar for films cycled in KOH solutions containing trace Fe and for films where Fe was coprecipitated with Ni during film deposition. With 10% coprecipitated Fe, Corrigan measures a Tafel slope of 25 mV dec$^{-1}$, similar to what is measured here (the activity per Ni site is compared quantitatively below).

We used the highest purity KOH available to prepare the 1 M KOH electrolyte which had <40 ppb Fe based on the lot analysis provided by the supplier. Fe impurities may also enter the solution from the glass electrochemical cell during exposure to basic solution. To determine the extent of Fe incorporation into the $Ni_yCo_{1-y}O_x$ films, the composition of the films before and after conditioning was analyzed by XPS and EPMA (Table 2). Both techniques indicate the presence of Fe in the conditioned $NiO_x$ and $Ni_yCo_{1-y}O_x$ films, consistent with Corrigan's work.[32] The amount of Fe incorporated also depended on the Ni content in the film; the $NiO_x$ films incorporated the most Fe, while Fe in the $CoO_x$ films was below the detection limit. These results suggest that Ni-containing films scavenge Fe from the solution. (This is

**Table 2. Fe Content of Thin Films**

| | Fe/(Ni + Co) | |
|---|---|---|
| conditioned sample | EPMA | XPS |
| $CoO_x$ | 0 | 0 |
| $Ni_{0.5}Co_{0.5}O_x$ | 0.034 | 0.11 |
| $NiO_x$ | 0.18 | 0.14 |
| $NiO_x$, electrolyzed KOH | 0.035 | 0.079 |

reminiscent of the high affinity of natural Fe(II)/Fe(III) hydroxides known as carbonated green rust for $Ni^{2+}$ in Fe-rich ocean waters,[41,42] which has been implicated in the oxygenation of ancient Earth's atmosphere.)[42,43] Pre-electrolysis of the KOH electrolyte solution (∼10 cm$^2$ Ni mesh anode and cathode, 1 week at 3 V) to remove Fe and other impurities reduced the quantity of Fe incorporation by roughly a factor of 2. A key result of these studies is therefore that the active catalyst material in the Ni-based films includes Fe (e.g., $Ni_yFe_{1-y}OOH$) and that the incorporation of Co limits its formation. As shown in Figure 8 and discussed below, direct

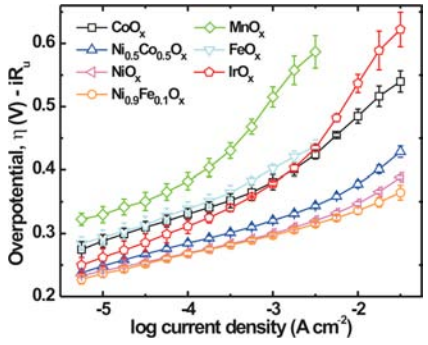


**Figure 8.** Comparison of steady-state Tafel measurements for ultrathin films synthesized in this study collected in 1 M KOH. Each data point represents a galvanostatic measurement held for at least 15 min and is the average of three different electrode samples (1 QCM and 2 Au/Ti-coated glass electrodes). Note that some error bars are smaller than the symbols.

synthesis of $Ni_{0.9}Fe_{0.1}O_x$ from the solution precursor increases slightly the activity of the catalyst film relative to the conditioned $NiO_x$ films. Understanding the detailed role of Fe in the OER mechanism as well as the possible differences between Fe incorporated during film deposition or during electrochemical conditioning are important directions for future studies.

**3.2. Thin Films as a System for Comparing Catalytic Activity of Metal Oxides.** The simplicity of the ultrathin film solution deposition coupled with the precise QCM film mass measurements enables direct comparison of different materials. Figure 8 shows Tafel measurements for several known OER catalysts prepared as films by solution deposition. Relevant values of catalytic activity derived from these Tafel measurements, including Tafel slope and the turnover frequency (TOF, defined as mol $O_2$ per mol metal per second), can be found in Table 3. Remarkably, the activity measured for the best catalyst studied here, $Ni_{0.9}Fe_{0.1}O_x$, is roughly 10-fold higher than that of $IrO_x$, which is traditionally considered to be one of the most active OER catalysts.[10] We note that the reported TOFs are lower limits because all of the deposited metal cations may, in some cases, not be in direct contact with the electrolyte. However, given that the films are on average only roughly 10


dx.doi.org/10.1021/ja307507a | J. Am. Chem. Soc. 2012, 134, 17253−17261

Table 3. Comparison of Metal Oxide Thin Film OER Activity[a]

| | $\eta$ @ 1 mA cm$^{-2}$ (mV) | dry film loading ($\mu$g cm$^{-2}$) | $J$ @ $\eta$ = 0.3 V (mA cm$^{-2}$) | mass activity @ $\eta$ = 0.3 V (A g$^{-1}$) | TOF (s$^{-1}$) @ $\eta$ = 0.3 V | Tafel slope (mV dec$^{-1}$) |
|---|---|---|---|---|---|---|
| $MnO_x$ | 514 ± 22 | 1.13 ± 0.08 | 0.002 ± 0.0009 | 1.8 ± 0.8 | 0.0004 ± 0.0002 | 49 ± 3 |
| $FeO_x$ | 405 ± 4 | 1.63 ± 0.08 | 0.012 ± 0.007 | 7.6 ± 4.5 | 0.0015 ± 0.0009 | 51 ± 3 |
| $IrO_x$ | 378 ± 4 | 4.12 ± 0.14 | 0.063 ± 0.036 | 15 ± 8.7 | 0.0089 ± 0.0050 | 49 ± 1 |
| $CoO_x$ | 381 ± 12 | 1.32 ± 0.14 | 0.020 ± 0.009 | 15 ± 6.8 | 0.0032 ± 0.0014 | 42 ± 1 |
| $Ni_{0.25}Co_{0.75}O_x$ | 341 ± 5 | 1.62 ± 0.09 | 0.079 ± 0.018 | 49 ± 11 | 0.0099 ± 0.0023 | 36 ± 1 |
| $Ni_{0.5}Co_{0.5}O_x$ | 320 ± 4 | 1.06 ± 0.08 | 0.30 ± 0.07 | 280 ± 70 | 0.056 ± 0.014 | 35 ± 2 |
| $Ni_{0.75}Co_{0.25}O_x$ | 312 ± 1 | 1.04 ± 0.09 | 0.47 ± 0.05 | 452 ± 64 | 0.089 ± 0.013 | 33 ± 1 |
| $NiO_x$ | 300 ± 3 | 1.13 ± 0.10 | 1.01 ± 0.22 | 896 ± 206 | 0.17 ± 0.04 | 29 ± 0.4 |
| $Ni_{0.9}Fe_{0.1}O_x$ | 297 ± 0.3 | 1.17 ± 0.14 | 1.24 ± 0.04 | 1065 ± 129 | 0.21 ± 0.03 | 30 ± 1 |

[a]See SI for a discussion of the origin and propagation of uncertainties.

monolayers thick and that they also likely contain sub-nm porosity resulting from the combusted organic surfactant used in the precursor solution, the reported TOFs are certainly less than a factor of 10 different from the true intrinsic values.

It is useful to compare the data measured in the thin-film electrode format with other measurements of catalyst activities. The active $Ni_yFe_{1-y}O_x$ samples derived from electrochemical conditioning of the thin film oxides are similar to the cathodically electrodeposited $Ni(OH)_2$ studied by Corrigan in the late 1980s.[31−33] Corrigan compared OER activities for $Ni(OH)_2$ with a variety of transition-metal ion additives in 1 M KOH and found that the addition of ∼10% Fe yielded the best performance.[32,33] At an overpotential of 287 mV, Corrigan measured a current of 0.1 A for 5.7 $\mu$mol of catalyst, equivalent to a TOF of 0.05 s$^{-1}$. Under the same conditions, we measured a similar TOF of 0.06 ± 0.01 s$^{-1}$ for the conditioned $Ni_yFe_{1-y}O_x$ thin film catalysts, supporting the hypothesis that the NiO catalysts studied here form Fe-containing hydroxide phases under OER conditions. More recently Merrill and Dougherty[44] and Li et al.[45] have also measured OER activity of electrodeposited $Ni_yFe_{1-y}(OH)_2$ similar to that reported by Corrigan. Direct comparison to that data, however, is not possible because the quantity of catalyst measured was not reported.

Recently there has been significant work on $CoO_x$-based catalysts for water oxidation in neutral to basic aqueous media. Surendranath et al. studied the water oxidation mechanism for $CoO_x$/phosphate (Co-Pi)[46] thin films with known Co content in near-neutral pH.[47] Based on these data, we calculate a TOF of 4 × 10$^{-5}$ s$^{-1}$ at $\eta$ = 300 mV. This is ∼80-fold slower than we find for $CoO_x$ and ∼5000-fold slower than the $Ni_{0.9}Fe_{0.1}O_x$. A key difference between these measurements is the electrolyte pH. Co-Pi operates at near-neutral pHs, which is advantageous for coupling to semiconductor absorbers that are unstable in basic or acidic media. Measurements made here were performed in 1 M KOH. Further studies are needed to quantify and understand the operation and stability of $Ni_{0.9}Fe_{0.1}O_x$ as a function of pH.

Yeo and Bell investigated $CoO_x$ and $Ni(OH)_2$ films electrodeposited onto roughened metal electrodes and reported that high work-function metals, such as Au, enhanced the $CoO_x$[48] and $Ni(OH)_2$[49] OER activity in 0.1 M KOH for the first few monolayers of deposited oxide. At $\eta$ = 350 mV, they found a TOF for 0.4 monolayers of $CoO_x$ on Au of 1.7 s$^{-1}$, much higher than the TOF measured for a thicker film (∼87 monolayers) of 0.06 s$^{-1}$. At $\eta$ = 350 mV, we found a lower limit TOF for the $CoO_x$ film (∼17 monolayer-equivalents calculated as in ref 48) of 0.050 ± 0.023 s$^{-1}$ assuming every Co was active, consistent with the findings of little support-induced activity enhancement beyond the first few $CoO_x$ monolayers observed by Yeo and Bell. For $Ni_{0.9}Fe_{0.1}O_x$, we found a TOF at $\eta$ = 350 mV of 2.8 s$^{-1}$ on the Au/Ti QCM crystals. Similar TOFs were measured for $Ni_{0.9}Fe_{0.1}O_x$ samples on ITO electrodes (Figure S12), demonstrating negligible enhancement from the Au support for the $Ni_{0.9}Fe_{0.1}O_x$ films measured here.

The measured TOFs can also be compared to those obtained for all-inorganic molecular catalysts, such as $[Co_4(H_2O)_2(PW_9O_{34})_2]^{10-}$ ($Co_4$POM), which appear to be the fastest known homogeneous water oxidation catalysts.[50] A TOF of 5 s$^{-1}$ for the $Co_4$POM cluster (or ∼1.3 s$^{-1}$ per Co) was measured at pH 8 using $Ru(bpy)_3^{3+}$ (bpy =2,2′-bipyridine) as a molecular oxidant ($E°$ = 1.24 V vs NHE, equivalent to $\eta$ = 480 mV).[51] We measured a TOF for the $CoO_x$ film at $\eta$ = 480 mV of 1.5 ± 0.3 s$^{-1}$, similar to that of the molecular catalyst.

$Ni_{0.9}Fe_{0.1}O_x$ studied here appears to be one of the most active OER catalysts in basic media known. The $Ni_{0.9}Fe_{0.1}O_x$ is superior to the $IrO_x$ control catalyst films synthesized in our lab with TOFs up to 2 orders of magnitude higher than $IrO_x$ depending on $\eta$ (Table 3 and Figure 8). These $IrO_x$ control films have a comparable activity to $IrO_2$ nanoparticles recently measured in 0.1 M KOH by Lee et al. using a controlled rotating disk technique.[52] Lee et al. found that at $\eta$ = 300 mV, ∼5 nm diameter $IrO_2$ particles had a mass activity of 11 A g$^{-1}$ and a specific surface area activity of 1.5 × 10$^{-5}$ A cm$^{-2}$. Assuming a surface Ir density of ∼1 × 10$^{15}$ cm$^{-2}$ (corresponding to the stable (110) surface), this yields a TOF at $\eta$ = 300 mV of 0.02 s$^{-1}$. We measured a similar mass activity of 15 A g$^{-1}$ and a lower-limit TOF (based on total Ir) of 0.009 s$^{-1}$ for the $IrO_x$ thin films. The agreement between these different measurements confirms the suitability of the $IrO_x$ films as controls for comparison to other catalysts. Hydrous $IrO_x$ nanoparticles have also been studied which appear to show higher OER activity.[14,53] From Tafel data reported for hydrous $IrO_x{\cdot}nH_2O$ nanoparticle films by Bediako et al., we calculate a TOF at $\eta$ = 300 mV of ∼0.4 s$^{-1}$ at pH = 12.5.[14] In that case, the electrochemically active sites are determined from the integrated charge of voltammetry sweeps. We found that these films were not stable at pH = 14 and therefore were unable to make a direct comparison of the TOF to the films studied here.

We can compare $Ni_{0.9}Fe_{0.1}O_x$ to the BSCF material reported recently by Suntivich et al., which was reported as one of the fastest known OER catalysts in basic media with specific surface-area activity 10-fold higher than $IrO_2$. The mass activity of the $Ni_{0.9}Fe_{0.1}O_x$ catalyst (∼10$^3$ A g$^{-1}$ at $\eta$ = 300 mV) is 100 times higher than that of the ball-milled BSCF nanoparticle


dx.doi.org/10.1021/ja307507a | J. Am. Chem. Soc. 2012, 134, 17253−17261

material measured in 0.1 M KOH at $\eta$ = 300 mV.[3] However, the BSCF nanoparticle size was large (~230 nm), with the interior of the particles inactive. It is more useful, therefore, to compare intrinsic activities, such as the TOF. At low overpotentials of ~300 mV, the BSCF has a TOF of ~0.6 $s^{-1}$, calculated based on the measured surface area and known crystal structure of the BSCF sample[54] and assuming only the Co/Fe cations are active (and the Sr/Ba inactive). This is similar to the lower-limit $Ni_{0.9}Fe_{0.1}O_x$ TOF of 0.21 $s^{-1}$, which was calculated based on the total Ni and Fe content of the film. At higher $\eta$, the $Ni_{0.9}Fe_{0.1}O_x$ catalyst appears superior due to the lower Tafel slope of ~30 mV $dec^{-1}$ compared to the BSCF Tafel slope of ~50 mV $dec^{-1}$.

The $Ni_{0.9}Fe_{0.1}O_x$ therefore has similar activity to the best reported previous catalysts (BSCF) and roughly an order of magnitude higher activity than precious metal $IrO_2$ catalysts in basic media. It contains only inexpensive earth abundant elements and can be easily deposited on arbitrary substrates by the solution method described here. One possible reason for the high activity of the NiOOH-based catalysts is that the catalytic activity occurs within the three-dimensional layered hydroxide/oxyhydroxide structure, which is different than typical solid materials, where catalysis occurs only at surface sites. The role of three-dimensional structure on the electrocatalytic properties is intriguing and a focus of our current studies in this area.

## 4. CONCLUSIONS

We developed a simple synthesis route to deposit OER catalysts of arbitrary composition as films only a few nm thick. The films were deposited on quartz crystal microbalance electrodes where the mass was measured and monitored *in situ* and the chemical/structural features of the films could be probed *ex situ* using surface analytical techniques. This provided a method to study the activity and electrochemical properties of heterogeneous electrocatalysts independent of other confounding factors associated with thick porous films. The method can be easily extended to other important systems, for example, heterogeneous electrocatalysts for $CO_2$ reduction.[55,56] By examining a series of metal oxide thin films, we found that $Ni_{0.9}Fe_{0.1}O_x$ is a more active OER catalyst than $IrO_2$ in basic media with similar activity to optimized BSCF perovskite catalysts.[3] We also found no evidence for a synergistic effect between Co and Ni oxides in the mixed oxide catalyst films, which is different from previous findings.[23−27,40] For all films containing Ni, we observed an *in situ* structural transformation from oxides to layered hydroxides/oxyhydroxides that correlates directly with increased catalytic activity, indicating that the layered hydroxide/oxyhydroxide catalysts are the active catalysts. The simple synthesis methods used here allow for the straightforward incorporation of the electrocatalysts with semiconductor photoelectrodes for sunlight-driven water splitting as well as for use in designer three-dimensional high-surface-area electrodes for optimized alkaline water electrolysis.

## ■ ASSOCIATED CONTENT

### Supporting Information

Figures S1−S12 and discussions of QCM $C_f$ calibration, trace impurity analysis by XPS, fitting of XPS data, and error analysis. This material is available free of charge via the Internet at http://pubs.acs.org.

## ■ AUTHOR INFORMATION


### Corresponding Author

swb@uoregon.edu


### Notes

The authors declare no competing financial interest.

## ■ ACKNOWLEDGMENTS

Support from the Center for Sustainable Materials Chemistry through NSF grant CHE-1102637 is acknowledged. This research was also supported by startup funds provided by the University of Oregon and the Oregon Nanoscience and Microtechnologies Institute (ONAMI). S.W.B. acknowledges support from the DuPont Young Professor Program. We acknowledge assistance from Stephen Golledge and Jason Fahrion (XPS), John Donovan (EPMA), Jeff Ditto and Kurt Langworthy (FIB), and Josh Razink (TEM) in The Center for Advanced Materials Characterization in Oregon (CAMCOR). CAMCOR analytical facilities are supported by grants from the W. M. Keck Foundation, the M. J. Murdock Charitable Trust, ONAMI, the Air Force Research Laboratory (under agreement no. FA8650-05-1-5041), NSF (grant no. 236200), and the University of Oregon.

## ■ REFERENCES


(1) Walter, M. G.; Warren, E. L.; McKone, J. R.; Boettcher, S. W.; Mi, Q.; Santori, E. A.; Lewis, N. S. *Chem. Rev.* **2010**, *110*, 6446.

(2) Cook, T. R.; Dogutan, D. K.; Reece, S. Y.; Surendranath, Y.; Teets, T. S.; Nocera, D. G. *Chem. Rev.* **2010**, *110*, 6474.

(3) Suntivich, J.; May, K. J.; Gasteiger, H. A.; Goodenough, J. B.; Shao-Horn, Y. *Science* **2011**, *334*, 1383.

(4) Trasatti, S.; Lodi, G. Oxygen and Chlorine Evolution at Conductive Metallic Oxide Anodes. In *Electrodes of Conductive Metallic Oxides*; Trasatti, S., Ed.; Elsevier: Amsterdam, The Netherlands, 1981; Vol. *B*; p 521.

(5) Matsumoto, Y.; Sato, E. *Mater. Chem. Phys.* **1986**, *14*, 397.

(6) Trasatti, S.; Petrii, O. A. *J. Electroanal. Chem.* **1992**, *327*, 353.

(7) Man, I. C.; Su, H.-Y.; Calle-Vallejo, F.; Hansen, H. A.; Martínez, J. I.; Inoglu, N. G.; Kitchin, J.; Jaramillo, T. F.; Nørskov, J. K.; Rossmeisl, J. *ChemCatChem* **2011**, *3*, 1159.

(8) Guerrini, E.; Consonni, V.; Trasatti, S. *J. Solid State Electrochem.* **2005**, *9*, 320.

(9) Hepel, T.; Pollak, F. H.; O'Grady, W. E. *J. Electrochem. Soc.* **1986**, *133*, 69.

(10) Trasatti, S. *J. Electroanal. Chem.* **1980**, *111*, 125.

(11) Rossmeisl, J.; Dimitrievski, K.; Siegbahn, P.; Nørskov, J. K. *J. Phys. Chem. C* **2007**, *111*, 18821.

(12) Rossmeisl, J.; Qu, Z.-W.; Zhu, H.; Kroes, G.-J.; Nørskov, J. K. *J. Electroanal. Chem.* **2007**, *607*, 83.

(13) Subbaraman, R.; Tripkovic, D.; Chang, K.-C.; Strmcnik, D.; Paulikas, A. P.; Hirunsit, P.; Chan, M.; Greeley, J.; Stamenkovic, V.; Markovic, N. M. *Nat. Mater.* **2012**, *11*, 550.

(14) Bediako, D. K.; Lassalle-Kaiser, B.; Surendranath, Y.; Yano, J.; Yachandra, V. K.; Nocera, D. G. *J. Am. Chem. Soc.* **2012**, *134*, 6801.

(15) Bockris, J. O.; Otagawa, T. *J. Phys. Chem.* **1983**, *87*, 2960.

(16) Bockris, J. O.; Otagawa, T. *J. Electrochem. Soc.* **1984**, *131*, 290.

(17) Suntivich, J.; Gasteiger, H. A.; Yabuuchi, N.; Shao-Horn, Y. *J. Electrochem. Soc.* **2010**, *157*, B1263.

(18) Trasatti, S.; Petrii, O. A. *Pure Appl. Chem.* **1991**, *63*, 711.

(19) Schweitzer, G. K.; Pesterfield, L. L. *The Aqueous Chemistry of The Elements*; Oxford University Press: Oxford, 2010; p 346−358.

(20) Sauerbrey, G. *Z. Phys. A: Hadrons Nucl.* **1959**, *155*, 206.

(21) Donovan, J. J.; Lowers, H. A.; Rusk, B. G. *Am. Mineral.* **2011**, *96*, 274.

(22) Phung, T. M.; Jensen, J. M.; Johnson, D. C.; Donovan, J. J.; McBurnett, B. G. *X-Ray Spectrom.* **2008**, *37*, 608.

(23) Wu, G.; Li, N.; Zhou, D.-R.; Mitsuo, K.; Xu, B.-Q. *J. Solid State Chem.* **2004**, *177*, 3682.
(24) de Chialvo, M. R. G.; Chialvo, A. C. *Electrochim. Acta* **1993**, *38*, 2247.
(25) Nikolov, I.; Darkaoui, R.; Zhecheva, E.; Stoyanova, R.; Dimitrov, N.; Vitanov, T. *J. Electroanal. Chem.* **1997**, *429*, 157.
(26) Cui, B.; Lin, H.; Li, J.-B.; Li, X.; Yang, J.; Tao, J. *Adv. Funct. Mater.* **2008**, *18*, 1440.
(27) Tiwari, S. K.; Samuel, S.; Singh, R. N.; Poillerat, G.; Koenig, J. F.; Chartier, P. *Int. J. Hydrogen Energy* **1995**, *20*, 9.
(28) Singh, R.-N.; Hamdani, M.; Koenig, J.-F.; Poillerat, G.; Gautier, J. L.; Chartier, P. *J. Appl. Electrochem.* **1990**, *20*, 442.
(29) Bocca, C.; Barbucci, A.; Delucchi, M.; Cerisola, G. *Int. J. Hydrogen Energy* **1999**, *24*, 21.
(30) Lian, K.; Thorpe, S. J.; Kirk, D. W. *Electrochim. Acta* **1992**, *37*, 169.
(31) Corrigan, D. A.; Knight, S. L. *J. Electrochem. Soc.* **1989**, *136*, 613.
(32) Corrigan, D. A. *J. Electrochem. Soc.* **1987**, *134*, 377.
(33) Corrigan, D. A.; Bendert, R. M. *J. Electrochem. Soc.* **1989**, *136*, 723.
(34) Wehrens-Dijksma, M.; Notten, P. H. L. *Electrochim. Acta* **2006**, *51*, 3609.
(35) McIntyre, N. S.; Cook, M. G. *Anal. Chem.* **1975**, *47*, 2208.
(36) Mitton, D. B.; Walton, J.; Thompson, G. E. *Surf. Interface Anal.* **1993**, *20*, 36.
(37) Biesinger, M. C.; Payne, B. P.; Lau, L. W. M.; Gerson, A.; Smart, R. S. C. *Surf. Interface Anal.* **2009**, *41*, 324.
(38) Chuang, T. J.; Brundle, C. R.; Rice, D. W. *Surf. Sci.* **1976**, *59*, 413.
(39) McIntyre, N. S.; Johnston, D. D.; Coatsworth, L. L.; Davidson, R. D.; Brown, J. R. *Surf. Interface Anal.* **1990**, *15*, 265.
(40) Rasiyah, P.; Tseung, A. C. C.; Hibbert, D. B. *J. Electrochem. Soc.* **1982**, *129*, 1724.
(41) Parmar, N.; Gorby, Y. A.; Beveridge, T. J.; Ferris, F. G. *Geomicrobiol. J.* **2001**, *18*, 375.
(42) Zegeye, A.; Bonneville, S.; Benning, L. G.; Sturm, A.; Fowle, D. A.; Jones, C.; Canfield, D. E.; Ruby, C.; MacLean, L. C.; Nomosatryo, S.; Crowe, S. A.; Poulton, S. W. *Geology* **2012**, *40*, 599.
(43) Konhauser, K. O.; Pecoits, E.; Lalonde, S. V.; Papineau, D.; Nisbet, E. G.; Barley, M. E.; Arndt, N. T.; Zahnle, K.; Kamber, B. S. *Nature* **2009**, *458*, 750.
(44) Merrill, M. D.; Dougherty, R. C. *J. Phys. Chem. C* **2008**, *112*, 3655.
(45) Li, X.; Walsh, F. C.; Pletcher, D. *Phys. Chem. Chem. Phys.* **2011**, *13*, 1162.
(46) Kanan, M. W.; Nocera, D. G. *Science* **2008**, *321*, 1072.
(47) Surendranath, Y.; Kanan, M. W.; Nocera, D. G. *J. Am. Chem. Soc.* **2010**, *132*, 16501.
(48) Yeo, B. S.; Bell, A. T. *J. Am. Chem. Soc.* **2011**, *133*, 5587.
(49) Yeo, B. S.; Bell, A. T. *J. Phys. Chem. C* **2012**, *116*, 8394.
(50) Yin, Q.; Tan, J. M.; Besson, C.; Geletii, Y. V.; Musaev, D. G.; Kuznetsov, A. E.; Luo, Z.; Hardcastle, K. I.; Hill, C. L. *Science* **2010**, *328*, 342.
(51) Jiao, F.; Frei, H. *Angew. Chem., Int. Ed.* **2009**, *48*, 1841.
(52) Lee, Y.; Suntivich, J.; May, K. J.; Perry, E. E.; Shao-Horn, Y. *J. Phys. Chem. Lett.* **2012**, *3*, 399.
(53) Nakagawa, T.; Bjorge, N. S.; Murray, R. W. *J. Am. Chem. Soc.* **2009**, *131*, 15578.
(54) Shao, Z. P.; Haile, S. M. *Nature* **2004**, *431*, 170.
(55) Kuhl, K. P.; Cave, E. R.; Abram, D. N.; Jaramillo, T. F. *Energy Environ. Sci* **2012**, *5*, 7050.
(56) Li, C. W.; Kanan, M. W. *J. Am. Chem. Soc.* **2012**, *134*, 7231.